

# Magnetic Structure and Properties of the Compositionally Complex Perovskite (Y<sub>0.2</sub>La<sub>0.2</sub>Pr<sub>0.2</sub>Nd<sub>0.2</sub>Tb<sub>0.2</sub>)MnO<sub>3</sub>: Supplementary Information

Nathan D. Arndt,<sup>a</sup> Brianna L. Musicó,<sup>b</sup> Kausturi Parui,<sup>a</sup> Keon Sahebkar,<sup>a</sup> Qiang Zhang,<sup>c</sup>  
Alessandro Mazza,<sup>d</sup> Megan Butala,<sup>a</sup> Veerle Keppens,<sup>b</sup> T. Zac Ward,<sup>d</sup> and Ryan F. Need<sup>a</sup>

## 1 Rietveld Refinement

The synchrotron X-ray diffraction (SXR) and neutron diffraction (ND) data were fit using GSAS-II.<sup>1</sup> Data refinement started with varying the data's histogram scale factor against the phase intensities from the input crystal information file (CIF). Input CIFs for refining the SXR were taken from the ICSD database. The SXR's background was fit with a 10 term Chebyshev-1 while the histogram scale factor was allowed to vary. The lattice parameters were then refined. A small secondary phase was noticed and indexed to YMnO<sub>3</sub>, this phase's CIF was added and then the histogram scale factor was turned off and the phase fraction scale factor was allowed to vary. A slight preferred orientation of the (5A)MnO<sub>3</sub> phase was seen in the (0K0) peak family and was fit using March-Dollase.<sup>2</sup> The peak shape was then fit by alternating refinements of the (5A)MnO<sub>3</sub> phase's isotropic displacement parameter and isotropic strain. There persisted a broadening of the peaks that March-Dollase preferred orientation nor isotropic micro-strain were able to wholly account for and is most likely due to nano-clustering that would need pair distribution function measurements to determine the scope of. To better account for this a generalized strain tensor model was used. This overall scheme was used for the SXR and ND refinements, with the small changes done in the ND refinement explained in that section. The goodness of fit metrics that are reported are  $wR$ , the weighted profile R-factor given by the equation  $R_w^2 = \sum_i w_i (y_{C,i} - y_{O,i})^2 / \sum_i w_i (y_{O,i})^2$ , and  $RF^2$ , the expected R-factor given by  $RF^2 = N / \sum_i w_i (y_{O,i})^2$ , where: are  $y_{O,i}$  is the original intensity value,  $y_{C,i}$  is the simulated intensity value, the weight is given by  $w_i = 1/\sigma^2[y_{O,i}]$ , and  $N$  is the number of data points.<sup>3</sup>

The fit to the SXR data will be shown, Fig. 1, with the refined values for the (5A)MnO<sub>3</sub> phase's site positions and lattice parameters shown in Table 1. This refinement was used as the starting point of the refinement of the ND patterns were the above process was followed. Since ND has greater sensitivity to O and between the ions on the A-site occupancy was of the A-site and the O sites was allowed to vary. The A-site occupancies each refined to a value of 0.2, or full occupancy, the two O's were able to improve the fit from an  $wR$  of 6.40% to an  $wR$  of 6.393% by refining to an occupancy value of 0.9915 and 1.0040, as this fit is not substantially different from the fit using 1 for both O occupancies all fits were done with 1 as the value. This refinement was then carried down to 9K only allowing the hydrostatic displacement to vary. At 60K and 9K a magnetic phase was needed to fit the pattern. The final, Fig. 5(a), is shown with the other plausible magnetic phases, Fig. 5(b-d). The magnetic moment refinement was checked for initialization errors and the results are in Table 7. The moments of the (5A)MnO<sub>3</sub> A-site magnetic ions were constrained to be equal so as to reduce the available fitting parameters from the three 0.2 occupancy magnetic ions (Pr<sup>3+</sup>, Nd<sup>3+</sup>, Tb<sup>3+</sup>) to one site with 0.6 occupancy of magnetic ions. This allowed the refinement to get a good fit to the data without over fitting. The shoulder of the magnetic peak centered at  $Q = 0.85\text{\AA}^{-1}$  was checked against the plausible magnetism for the YMnO<sub>3</sub> phase and the fit is shown in Fig. 7.

<sup>a</sup> Department of Materials Science and Engineering, University of Florida, Gainesville, Florida 32611, USA. E-mail: rneed@ufl.edu

<sup>b</sup> Department of Materials Science and Engineering University of Tennessee Knoxville, TN 37996-4545, USA.

<sup>c</sup> Neutron Science Division Oak Ridge National Laboratory Oak Ridge, TN 37831, USA.

<sup>d</sup> Materials Science and Technology Division Oak Ridge National Laboratory Oak Ridge, TN 37831, USA.

## 1.1 SXR D Rietveld Refinement

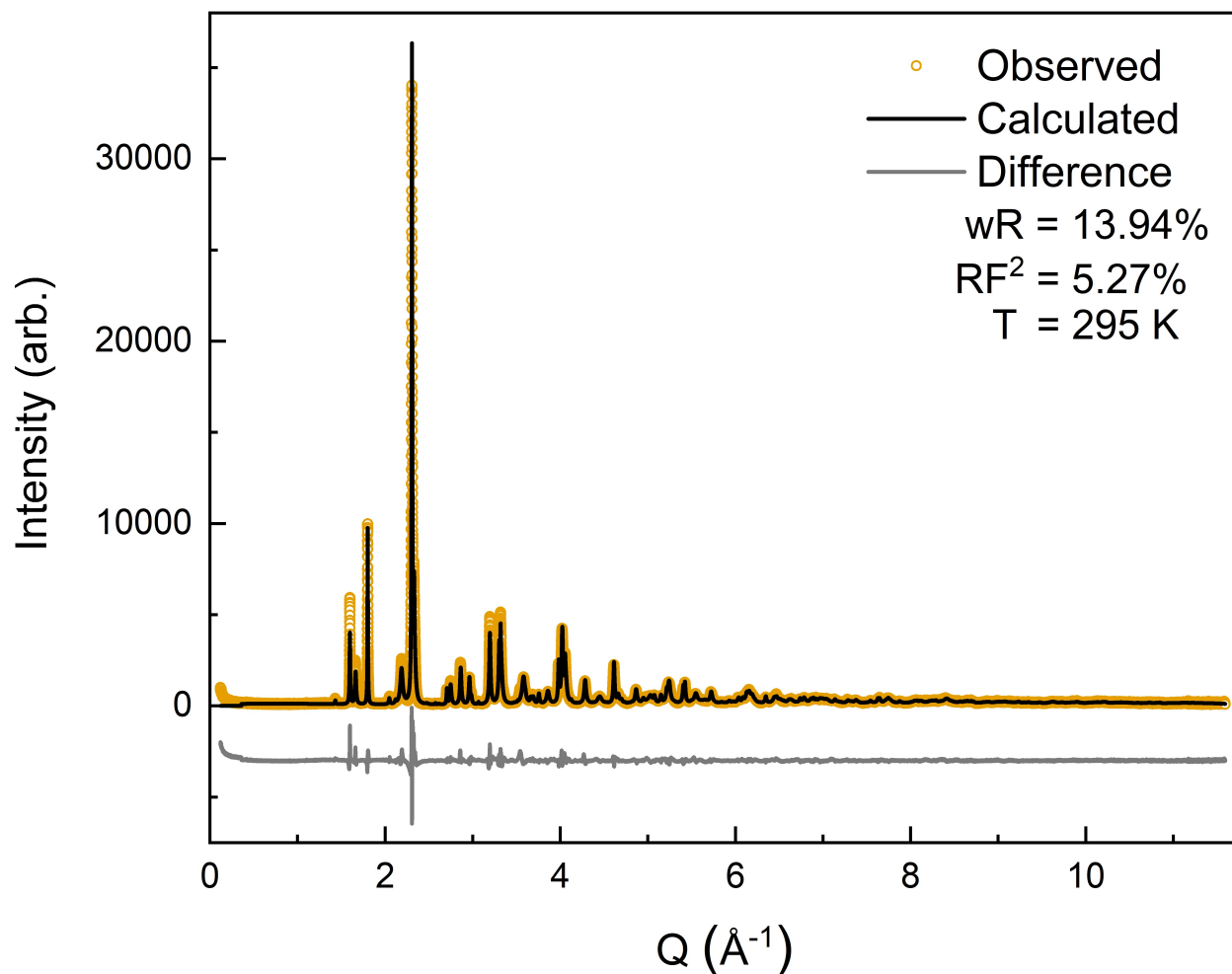


Figure 1: Full  $Q$  range of the SXR D refinement with the observed data shown by orange circles, the fit shown as a solid black line, and the difference, ( $Data - Fit$ ) shifted down for visibility, curve shown as a gray line. The  $wR$  of the fit is 13.94% and the  $(5A)MnO_3$   $RF^2$  is 5.27%.

Table 1: Crystal structure parameters of  $(5A)MnO_3$  at room temperature refined from the SXR D data.

Atoms	$x$	$y$	$z$	$U_{iso}$
A-site 4c	0.06566	0.25	0.98952	0.0111
Mn 4b	0	0	0.5	0.0078(5)
O1 4c	0.46974	0.25	0.08918	0.0029
O2 8d	0.18414	0.54946	0.20827	0.0015
Unit Cell (Å)	$a = 5.74388(9)$	$b = 7.55468(7)$	$c = 5.39151(6)$	Volume = 233.9548(26)
	$Rw = 13.94$	$RF^2_{5A} = 5.27$	$RF^2_{YMnO_3} = 35.66\%$	Temperature = 300 K

## 1.2 Nuclear Refinement

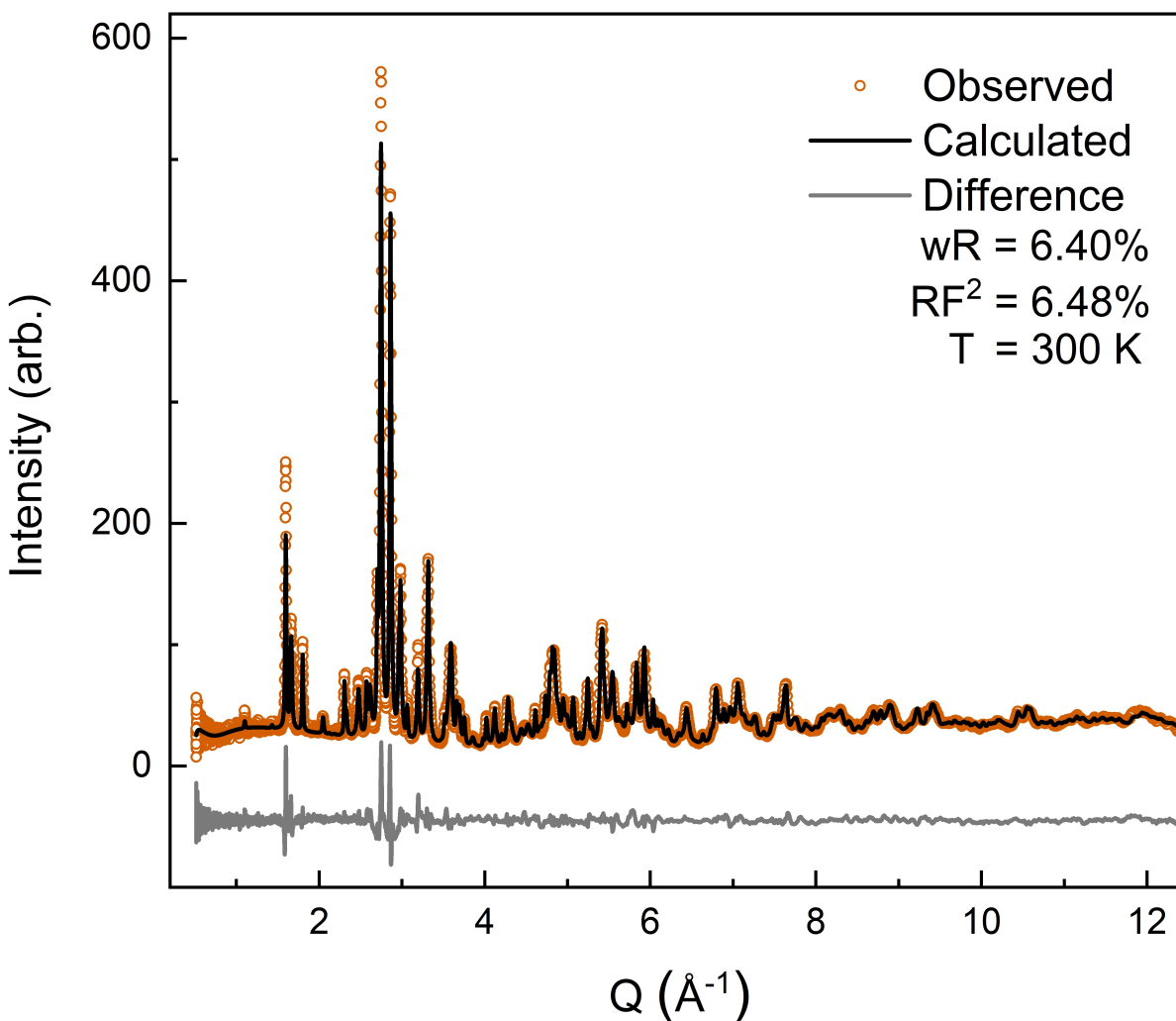


Figure 2: Full  $Q$  range of the 300 K ND refinement with the observed data shown by burnt orange circles, the fit shown as a solid black line, and the difference curve shown as a gray line, ( $Data - Fit$ ) shifted down for visibility. The  $wR$  of the fit is 6.40% with the  $m(5A)MnO_3$   $RF^2$  is 6.48%.

Table 2: Structural parameters from Rietveld refinements of NPD at room temperature pattern shown in Fig. 2

Atoms	$x$	$y$	$z$	$U_{iso}$
A-site 4c	0.06735(30)	0.25	0.9896(4)	0.00929(29)
Mn 4b	0	0	0.5	0.0078(5)
O1 4c	0.4762(4)	0.25	0.0867(3)	0.0104(4)
O2 8d	0.18351(27)	0.54537(18)	0.21109(25)	0.00864(23)
Unit Cell (Å)	$a = 5.74825(9)$	$b = 7.5502(5)$	$c = 5.39195(4)$	Volume = 234.015
	$Rw = 6.397$	$RF^2_{5A} = 6.484$	$RF^2_{YMnO_3} = 31.638$	Temperature = 300 K

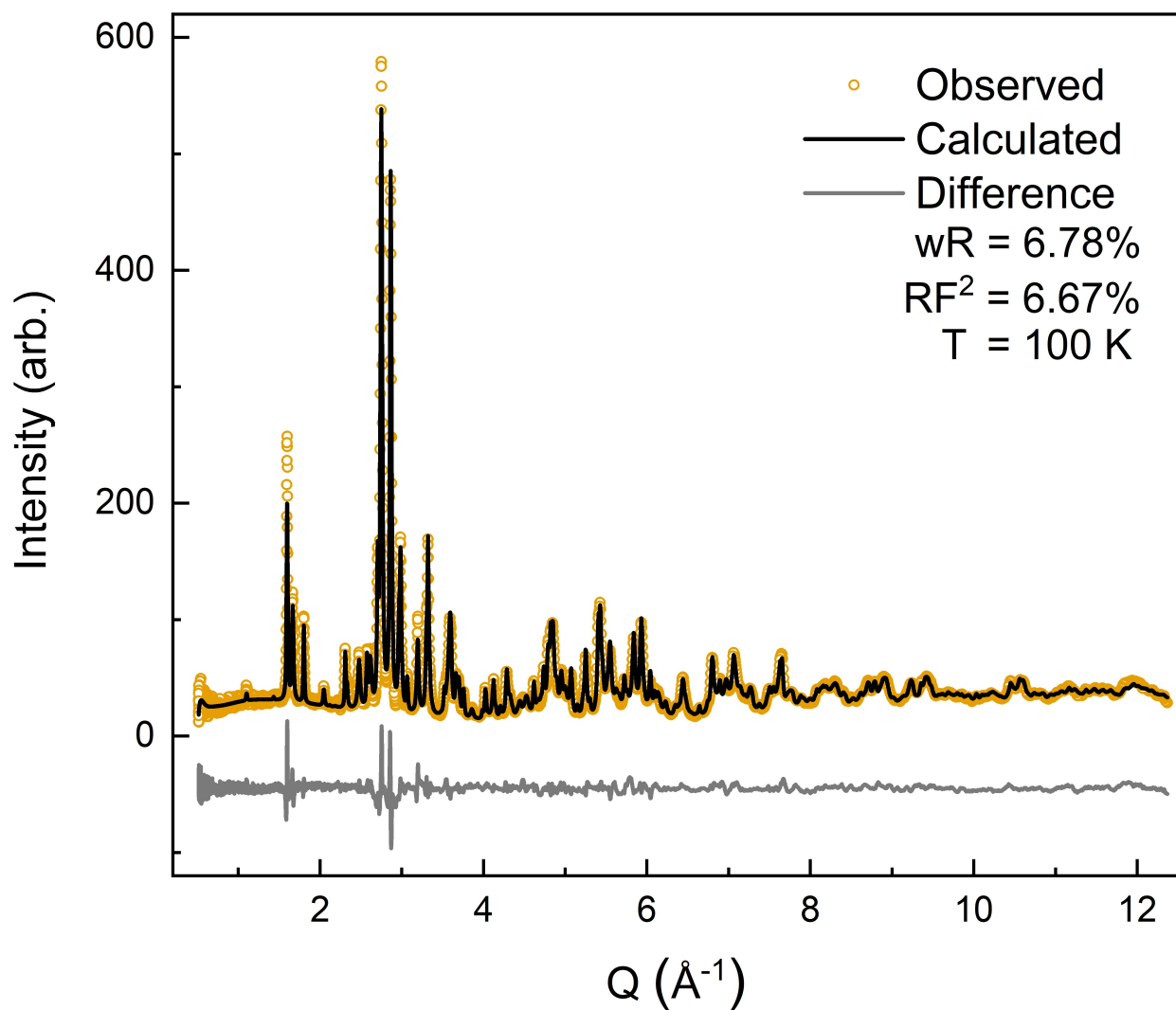


Figure 3: Full  $Q$  range of 100K ND refinement with the observed data shown by yellow circles, the fit shown as a solid black, and the difference curve shown as a gray line, ( $Data - Fit$ ) shifted down for visibility. The  $wR$  of the fit is 6.78% and the  $(5A)MnO_3$   $RF^2$  is 6.67%.

Table 3: Rietveld refinements of NPD at 100K, the pattern is shown in Fig. 3. Only the hydrodynamic strain was allowed to vary

Unit Cell ( $\text{\AA}$ )	$a = 5.74405$	$b = 7.53715$	$c = 5.38850$	Volume = 233.288
	$Rw = 6.783\%$	$RF^2_{5A} = 6.673\%$	$RF^2_{MnO_3} = 32.453\%$	Temperature = 100 K

### 1.3 Magnetic Refinement

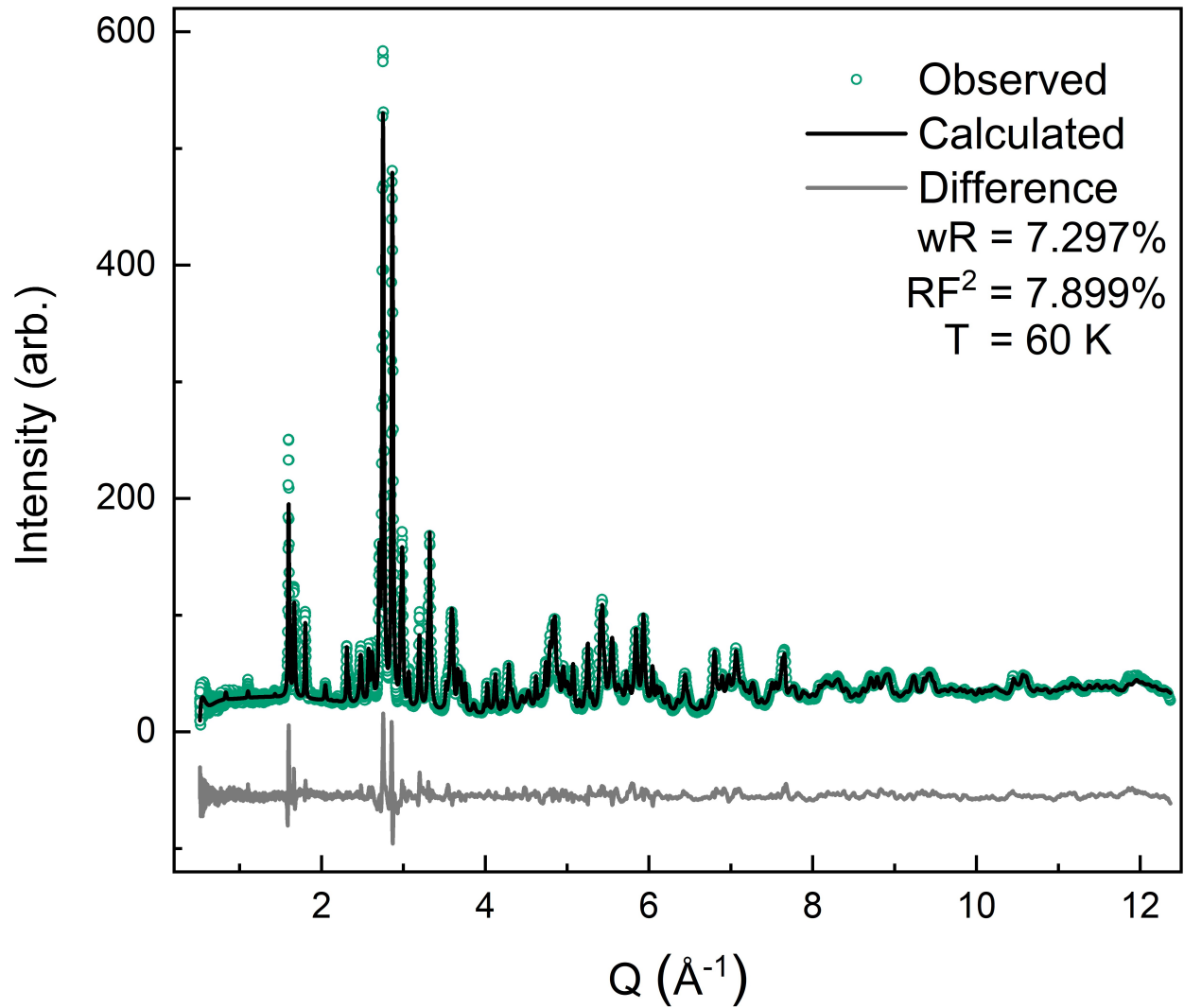


Figure 4: Full  $Q$  range of the 60K ND refinement with the observed data shown by green circles, the fit shown as a solid black line, and the difference curve shown as a gray line scaled,  $(Data - Fit)$  shifted down for visibility. The  $wR$  of the fit is 7.297% and the  $(5A)MnO_3$   $RF^2$  is 7.899%.

Table 4: Rietveld refinement of ND at 60K, the pattern is shown in Fig. 4. Only the hydrodynamic strain was allowed to vary in the crystallographic phase, the moment value was allowed to vary in the  $(5A)MnO_3$  magnetic phase.

Unit Cell (Å)	$a = 5.74202$	$b = 7.53592$	$c = 5.38908$	Volume = 233.288
	$Rw = 7.297\%$	$RF^2_{5A} = 7.899\%$	$RF^2_{MnO_3} = 23.962\%$	Temperature = 60 K
Magnetic Moments	$m_x$	$m_y$	$m_z$	Modulus
$Mn^{3+}$	0.3464	0.5005	0.1458	0.6259
A-site	-	0.0	-	0

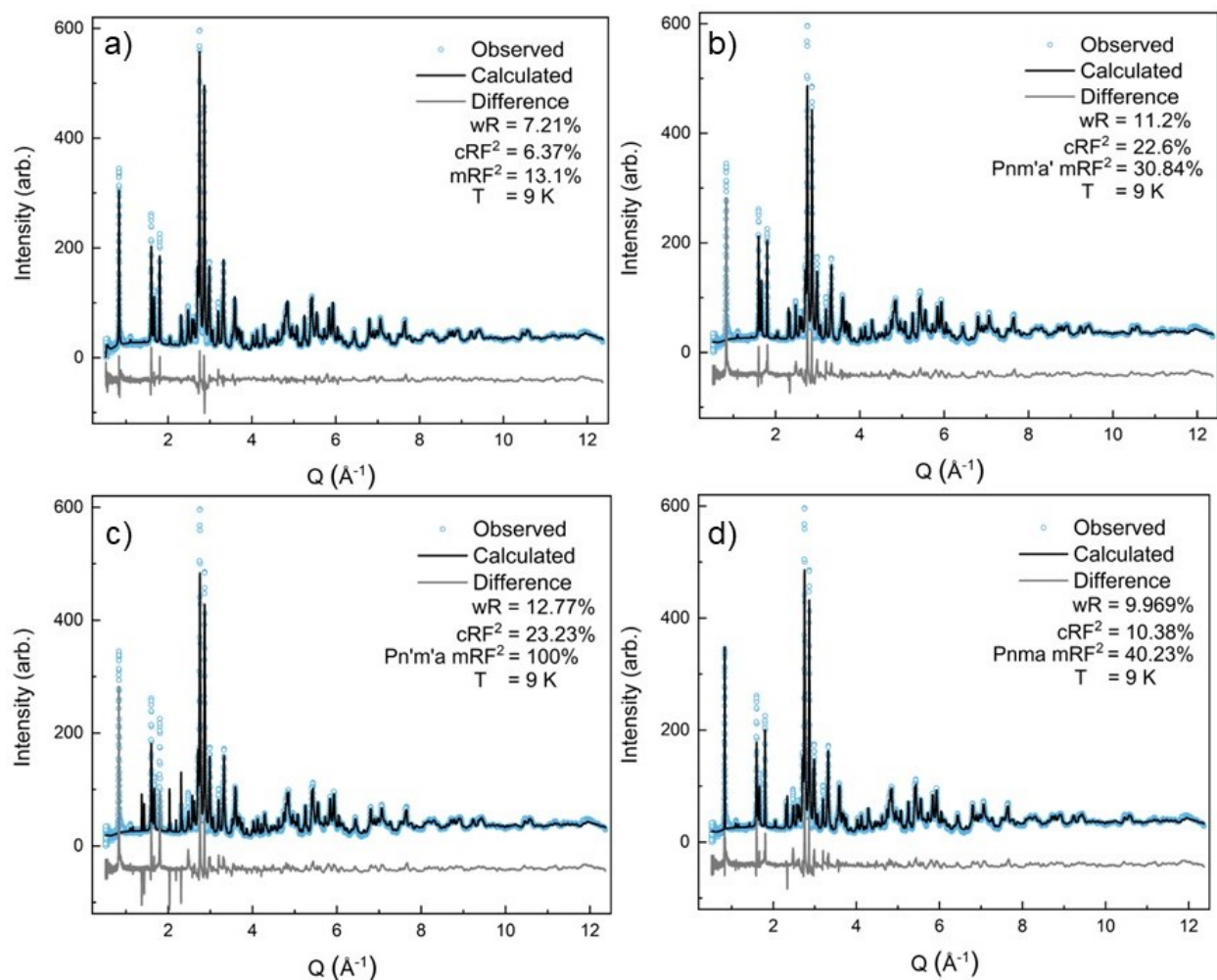


Figure 5: Full  $Q$  range of ND pattern taken at 9K with the circles of light blue showing the observed data, the black line denoting the fit and the light gray line being the difference, ( $Data - Fit$ ) shifted down for visibility. The four plausible magnetic structures were  $Pn'm'a'$ ,  $Pnm'a'$ ,  $Pn'm'a$ , and  $Pnma$ , for completeness all were refined against the observed data. (a)  $Pn'm'a'$  is the best fit as it adds no extraneous peaks while capturing most of the intensity of the magnetic peaks. (b)  $Pnm'a'$  this misses the antiferromagnetic peak at low  $Q$  but does capture the ferromagnetic addition to the nuclear peaks. (c)  $Pn'm'a$  misses the antiferromagnetic peak at low  $Q$  as well as the ferromagnetic addition to the nuclear peaks. (d)  $Pnma$  is able to capture the antiferromagnetic peak but as this magnetic structure has less symmetry then the others weight is added to peaks between the (010) and the (101) that are not seen in the observed data. The Table 5 shows the goodness of fit values for each refinement.

Table 5: Rietveld refinement of ND at 9K with differing magnetic structures, the patterns are shown in Fig. 5. The structural components were fit and then held the same as the differing magnetic structures were brought in and then the magnetic moments were allowed to vary.

	$Pn'm'a'$	$Pnm'a'$	$Pn'm'a$	$Pnma$
$wR$	7.21%	11.198%	12.774%	9.969%
$RF_{SA}^2$	6.367%	22.598%	23.232%	10.375
$RF_{YMnO_3}^2$	10.263%	80.913%	81.467%	27.383
$RF_{Mag}^2$	13.070%	30.840%	100.00%	40.232%
(010) peak	yes	no	no	yes

Table 6: Rietveld refinement of ND at 9 K, the pattern is shown in Fig. 5(a). Only the hydrodynamic strain was allowed to vary in the crystallographic phase, the moment values were allowed to vary in the (5A)MnO<sub>3</sub> magnetic phase.

Unit Cell (Å)	$a = 5.74018$	$b = 7.53438$	$c = 5.39047$	Volume = 233.131
$Rw = 7.21\%$	$RF^2_{5A} = 6.37\%$	$RF^2_{YMnO_3} = 10.25\%$	$RF^2_{Pn'ma'} = 13.1\%$	Temperature = 9 K
Magnetic Moments	$m_x$	$m_y$	$m_z$	Modulus
Mn <sup>3+</sup>	1.9981	0.5473	0.1152	2.0749
A-site	-	1.309309517	-	1.309309517

Table 7: Magnetic initialization table, by symmetry the A-site can only have a moment in the y-direction, listed A-site moment is on 60% of the site

Initialization	$m_x$	$m_y$	$m_z$	Modulus
Mn <sup>3+</sup> (100)	-1.971452416	0.34795043	-0.101439255	2.004490971
A-site (010)	-	1.273395863	-	1.273395863
Mn <sup>3+</sup> (-100)	-1.971859373	0.349296712	-0.09277917	2.004705853
A-site (0-10)	-	1.274734329	-	1.274734329
Mn <sup>3+</sup> (111)	-1.916838888	0.232781494	-0.168813173	1.938286985
A-site (010)	-	1.27521698	-	1.27521698
Mn <sup>3+</sup> (-1-1-1)	-1.987527221	0.190110124	0.232497465	2.010089895
A-site (0-10)	-	1.381197337	-	1.381197337
Mn <sup>3+</sup> (333)	-1.987145412	0.196853506	-0.256497398	2.013278199
A-site (030)	-	1.352939975	-	1.352939975
Mn <sup>3+</sup> (-3-3-3)	-1.978902882	0.287464669	-0.175679489	2.00737536
A-site (0-30)	-	1.298372622	-	1.298372622
Mn <sup>3+</sup> Average	-1.968954365	0.267409489	-0.09378517	1.989242264
A-site Average	-	1.309309517	-	1.309309517

## 1.4 Fitting the (010) Magnetic Peak Tail

Figure 6 shows the 9K ND data zoomed in on the (010) magnetic peak and its high  $Q$  tail. The high- $Q$  tail was analyzed in two ways corresponding to two hypothetical origins: (1) magnetic order in the  $\approx 1$  wt%  $\text{YMnO}_3$  impurity and (2) a small weight fraction of a second  $Pnma$  phase with a contracted  $b$ -axis.

For the first scenario, reviewing and indexing reported  $\text{YMnO}_3$  magnetic structures<sup>4-6</sup> resulted in only one possible match to the high- $Q$  tail, the triangular AFM structure,  $P6_3'mc'$ . However, including the reported  $P6_3'mc'$  structure in the refinement did not meaningfully change the overall goodness-of-fit or phase-specific  $RF^2$  values. This is because, as shown in Fig. 7, the magnetic intensity from  $\text{YMnO}_3$  at the high- $Q$  tail position was limited by the size of  $\text{YMnO}_3$ 's largest nuclear peak at  $Q = 1.102 \text{ \AA}^{-1}$ . In addition, adding  $P6_3'mc'$  to the refinement placed an extraneous peak at  $Q = 0.684 \text{ \AA}^{-1}$ , which is not present in our data. It is possible that this is not the correct magnetic phase for our  $\text{YMnO}_3$  impurity, which would allow the magnetic-to-nuclear structure factor ratios to change and perhaps fit the high- $Q$  tail better. However, the  $\text{YMnO}_3$  magnetic structure cannot be refined from the one nuclear and one magnetic reflection present in our data.

To consider the second scenario, where the high- $Q$  tail originates from a small fraction of the main phase,  $(5A)\text{MnO}_3$ , with a smaller  $b$ -axis, we compared the peak shape of the purely magnetic (010) to the related (020) and (040) peaks that have mixed nuclear and magnetic character. Peak fitting was done using Igor Pro's multipeak fit package using constant (flat) backgrounds over the plotted region to minimize the number of free parameters. Figure 8 shows the best fit of the (010) peak, which required two peaks in order to fit well.

The (020) and (040) were analyzed by first taking the peak positions determined for the (010) and scaling them to the higher order reflections. The peak centers were fixed while their intensity and width were allowed to fit. As shown in Figure 9, the (020) does not show any visible evidence of a second nuclear phase and is best fit with only a single peak. Forced inclusion of a second peak corresponding to the high- $Q$  tail result in negative intensity or a shift of the primary peak off the data's peak center. The (040) peak structure, shown in Figure 10(a), is far more complicated as it overlaps with several other peaks from the  $(5A)\text{MnO}_3$  and  $\text{YMnO}_3$  phases. Notably, there is a small peak, denoted with an asterisk, that is close to the calculated high- $Q$  tail position of the (010) scaled to the (040). However, as shown in Fig. 10(b-d), the small weight of this peak combined with the extra parameters from the other peaks in the area make fitting this possible (040) high- $Q$  tail difficult and it usually refines to have zero or negative intensity. All higher order  $(0K0)$  peaks have similar peak overlap problems and lower intensity. Therefore, this analysis is ultimately inconclusive. However, the absence of any peak intensity at high- $Q$  tail position of the (020) suggests this scenario is also wrong, and there is *not* an appreciable amount of  $(5A)\text{MnO}_3$  with a small  $b$ -axis. As noted in the main text, this leave short-range magnetic order along the  $b$ -axis as a possible explanation. However, new measurements sensitive to short-range magnetic order are needed to answer that question and confirm the origin of the high- $Q$  tail observed on the magnetic (010) peak.

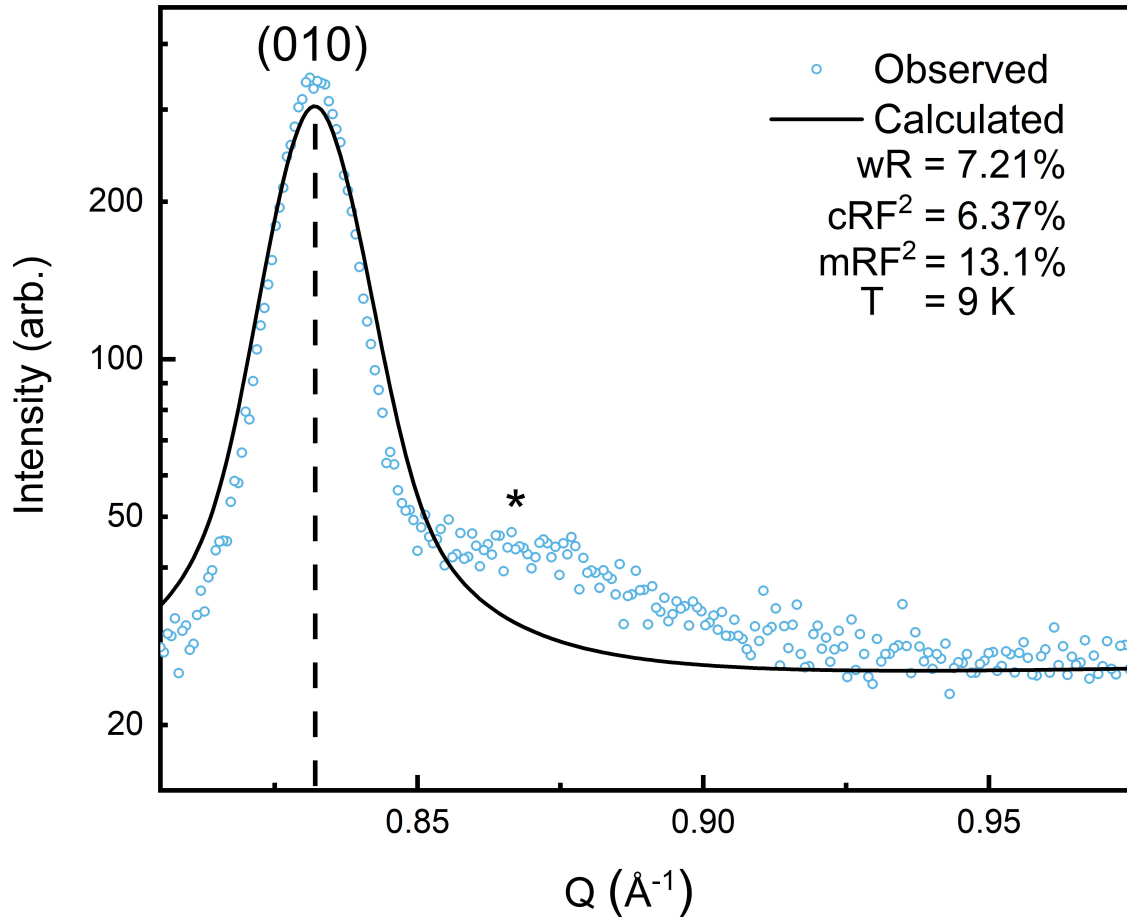


Figure 6: The 9K ND pattern has an asymmetric peak at the  $Pn'ma'$  (010) AFM reflection,  $Q = 0.83197$ . This figure is a zoom into the area around that peak showing the observed data with the circles of light blue showing the observed data and the black line denoting the fit. The uncaptured higher  $Q$  tail is marked with, \*, to draw the eye. The intensity is plotted log scale as a visual aid.

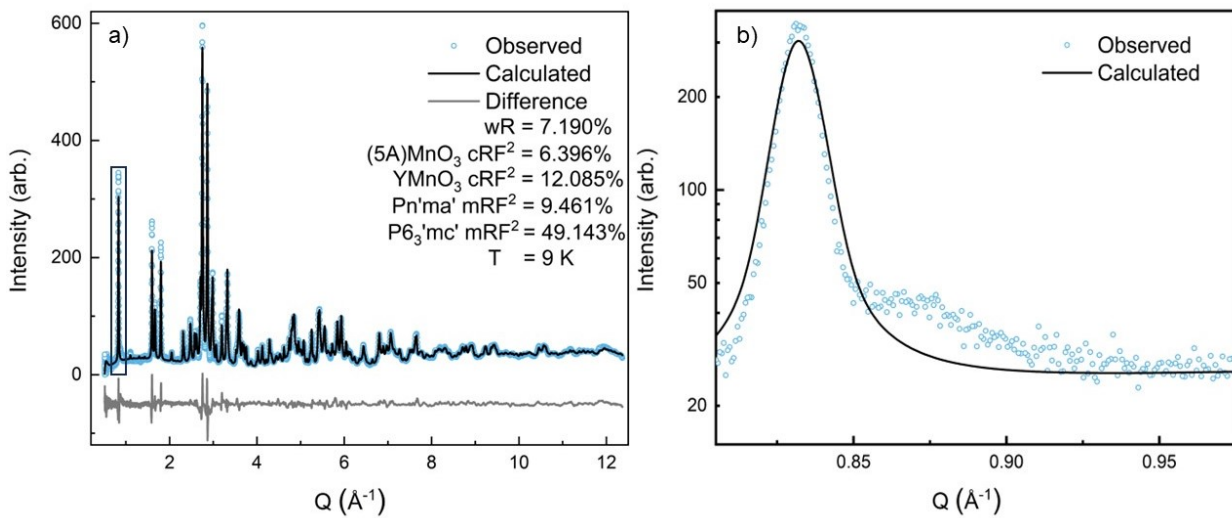


Figure 7: Checking the plausible magnetic structure of  $YMnO_3 P6_3'mc'$  on the fit of the 9K ND data. (a) Full  $Q$  range of ND pattern taken at 9K with the circles of light blue showing the observed data, the black line denoting the fit and the light gray line being the difference,  $(Data - Fit)$  shifted down for visibility. (b) No noticeable difference on the weighting is seen on the high  $Q$  shoulder of the peak at  $Q \approx 0.83$ , nor anywhere else in the diffraction pattern.

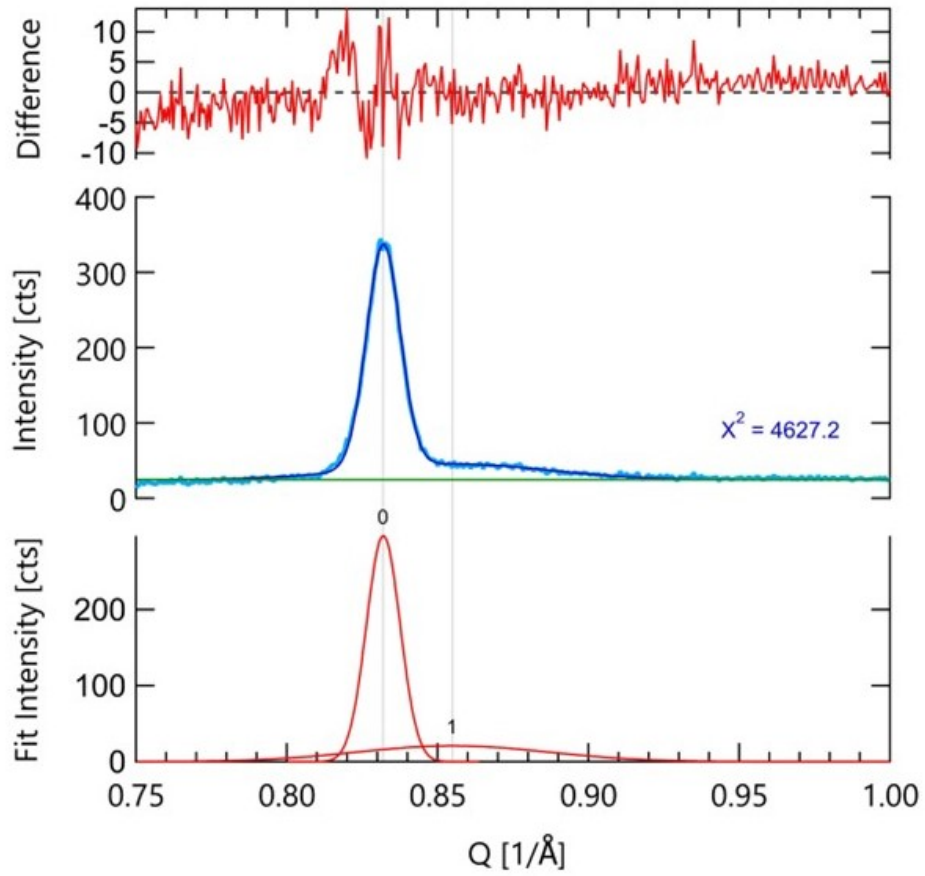


Figure 8: Igor multipeak fit of the (010) magnetic peak and its high  $Q$  shoulder. The light blue line shows the observed data in the middle panel, the bottom panel shows the fit as two peaks one centered on the (010) reflection at  $Q = 0.83197 \text{ \AA}^{-1}$  and its shoulder centered at  $Q = 0.85499 \text{ \AA}^{-1}$ , and the top panel shows the difference curve. The asymmetry of the (010) peak is the largest source of residual with the fit achieving  $\chi^2 = 4627.3$ .

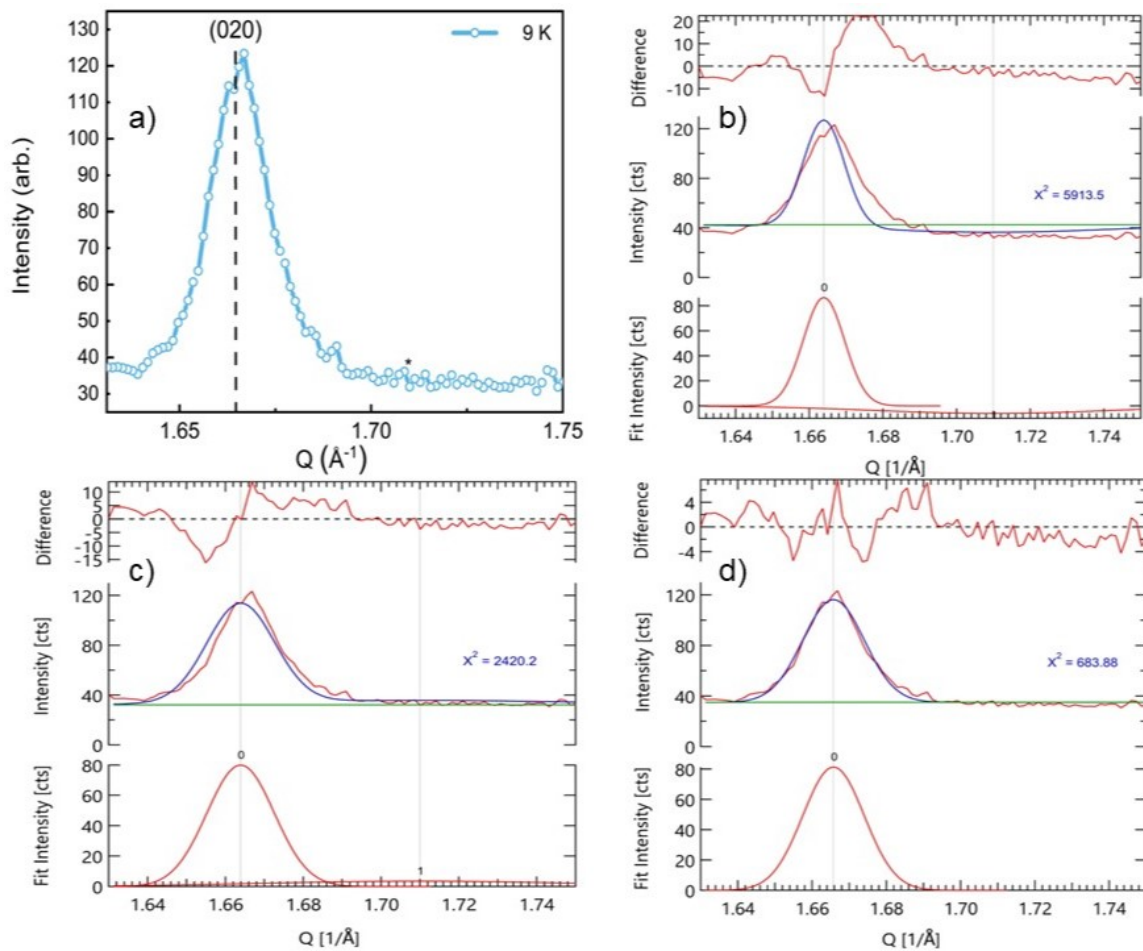


Figure 9: (a) The observed intensity from the 9 K ND diffraction is plotted around the (5A)MnO<sub>3</sub> (020) reflection. The calculated position of the high  $Q$ -tail should be is shown with an \*. (b-d) Igor fit of the (020) peak using two peaks whose position and widths have been determined from the fit of (010) AFM peak. (b) The amplitude of the two peaks was allowed to fit while holding the position and widths to the calculated values, with these constraints a good fit,  $\chi^2 = 5913.5$ , is not possible and the amplitude of the smaller  $b$ -axis peak achieves a negative value. (c) The amplitude and width of the two peaks was allowed to fit while the position was held to calculated values. This obtained a better fit with all values remaining physical but the fit does not capture all of the main peaks shape and weight,  $\chi^2 = 2420.2$ . (d) The amplitude, width, and position of the two peaks were fit, this fit achieved a good result,  $\chi^2 = 683.88$ , but only after it removed the secondary peak.

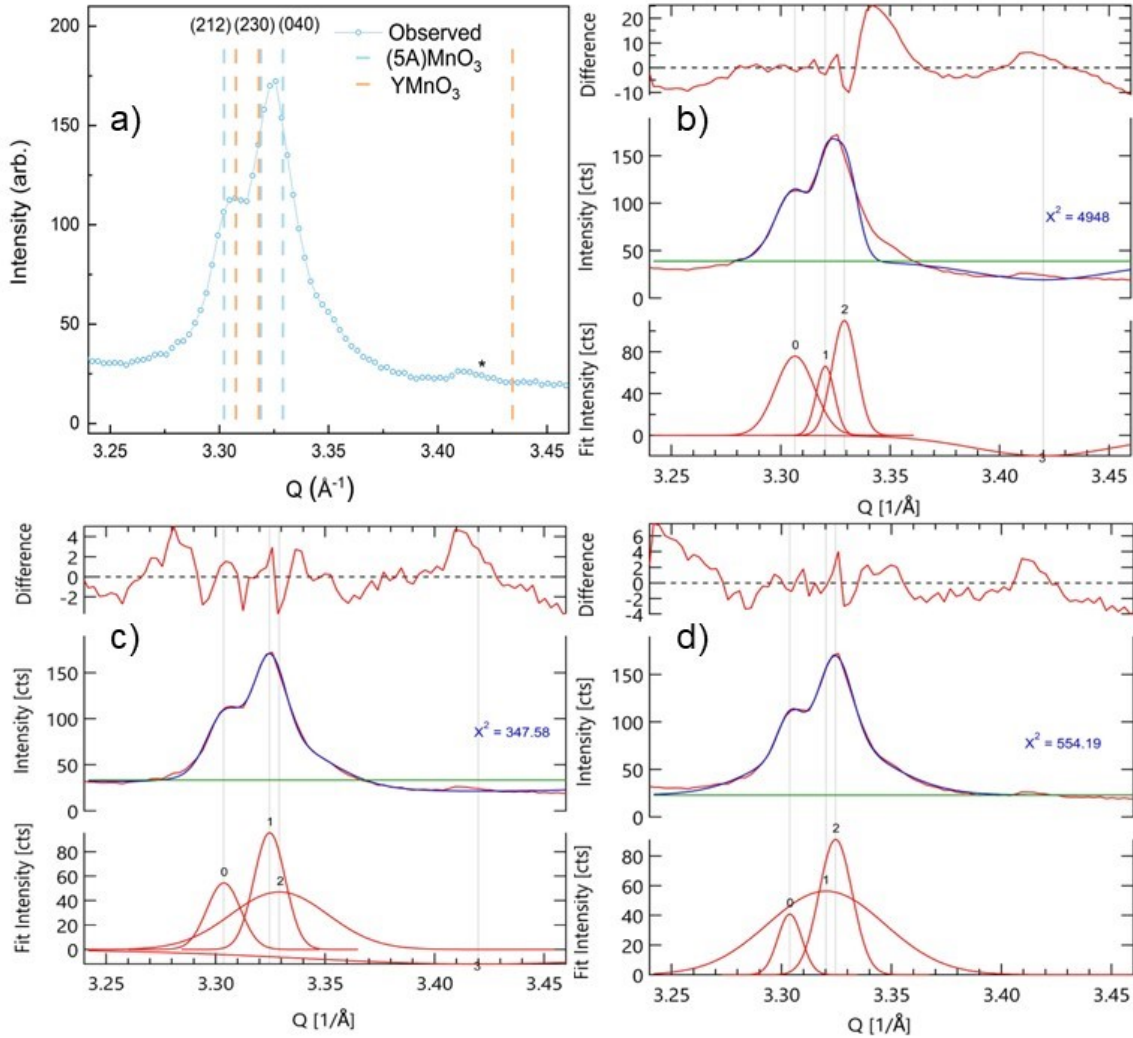


Figure 10: (a) Shows the position of the (040) (5A)MnO<sub>3</sub> reflection, these are labeled above, unlike the (010) and (020) peak the (040) peak has many peaks with close  $d$ -spacing. The calculated position of the smaller  $b$ -axis (040) peak is denoted by the \*, as can be seen there is a small bit of extra weight here that is not associated with any other peaks. (b-d) Igor fits of the (040) peak using two peaks whose position and widths have been determined from the fit of (010) AFM peak. The non-(040) peaks were allowed to vary in each refinement. (b) The amplitude of the two peaks was allowed to fit while holding the position and widths to the calculated values, with these constraints a good fit,  $\chi^2 = 4948$ , is not possible and the amplitude of the smaller  $b$ -axis peak achieves a negative value. (c) The amplitude and width of the two peaks was allowed to fit while the position was held to calculated values. This fit had the small  $b$ -axis peak achieve a negative width and amplitude, this fits the data well but is non-physical,  $\chi^2 = 347.58$ . (d) The amplitude, width, and position of the two peaks were fit, this fit achieved a good result,  $\chi^2 = 554.19$ , but only after it removed the secondary peak.

## 2 Bulk Magnetization

Determination of the magnetic transition temperatures was done using numerical differentiation and linear regression fits implemented in the Igor Pro 9 software package. An example is shown in Fig. 12, using the field cooled (FC)  $H = 100\text{Oe}$  data.

Figure 13 shows the 10K zero-field cooled (ZFC) magnetization versus applied field (MvH) compared to the 10K FC MvH at  $\pm 70\text{kOe}$  to fully illustrate the exchange bias that is seen at 10K. The average exchange bias field that is seen is 31 Oe.

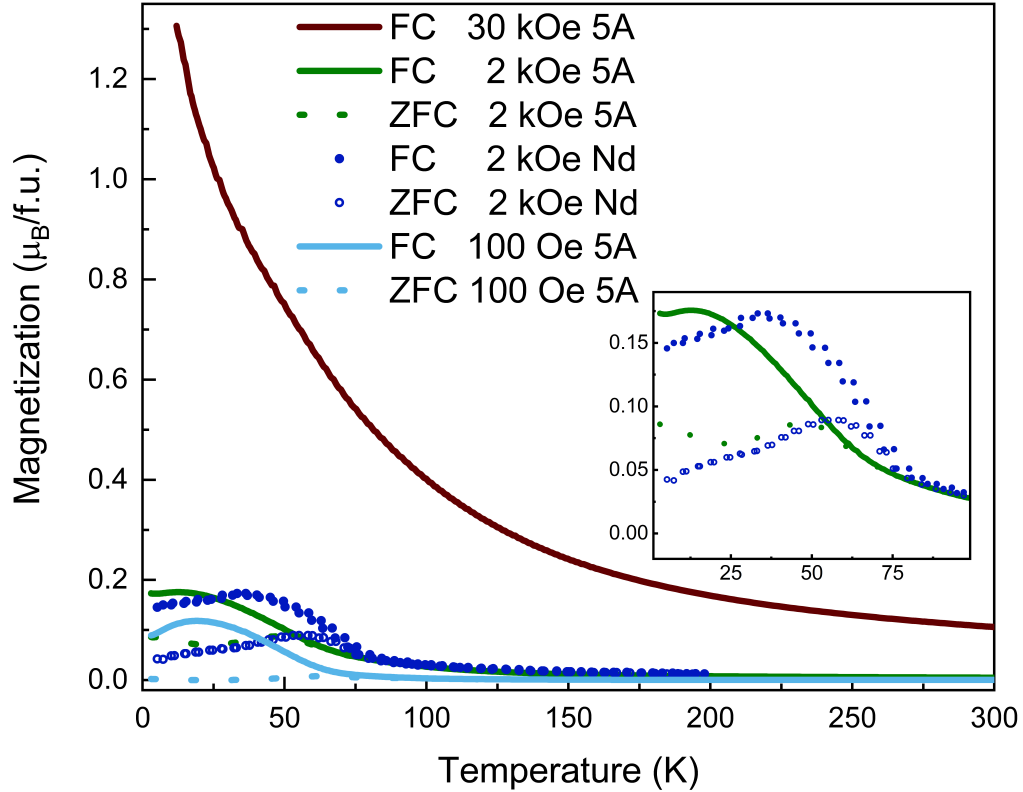


Figure 11: Full MvT's of the  $(5A)\text{MnO}_3$  at 100Oe, 2kOe, 30kOe we have reproduced the  $H = 2\text{kOe}$  MvT from Muñoz, *et al.*<sup>7</sup> in the blue open (ZFC) and closed (FC) circles. The inset shows a comparison of the  $(5A)\text{MnO}_3$  vs the  $\text{NdMnO}_3$  at  $H = 2\text{kOe}$  from 2K to 100K.

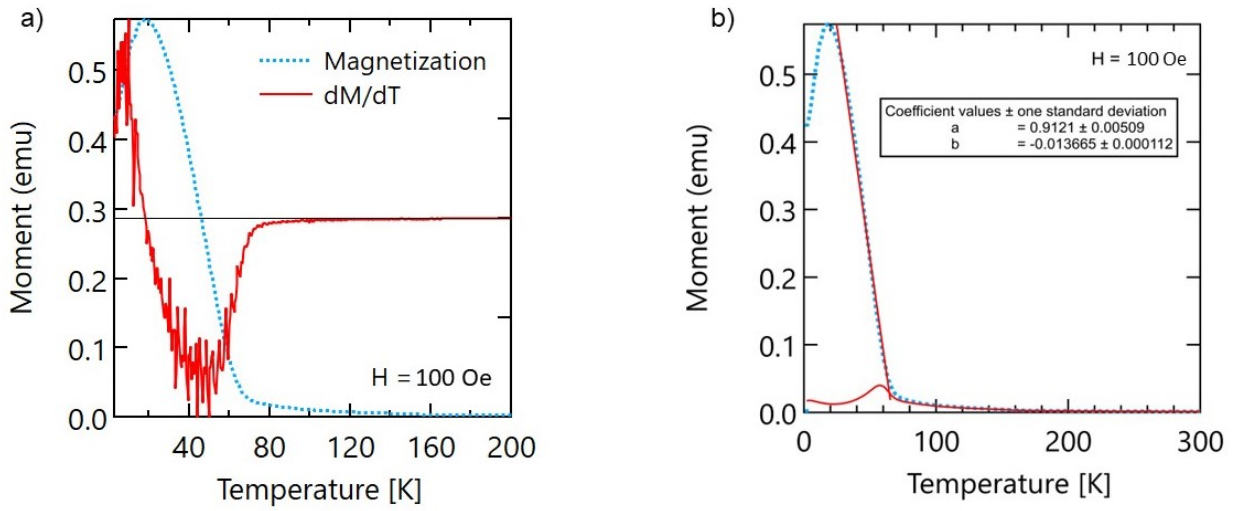


Figure 12: (a) The 100Oe FC data and its numerical derivation are shown, from this the ordering temperature for the A-site was able to be determined,  $T_{A\text{-site}}=18$  K. (b) A linear regression was fit to the slope from the first ordering temperature to the second and was used to determined to be 67 K.

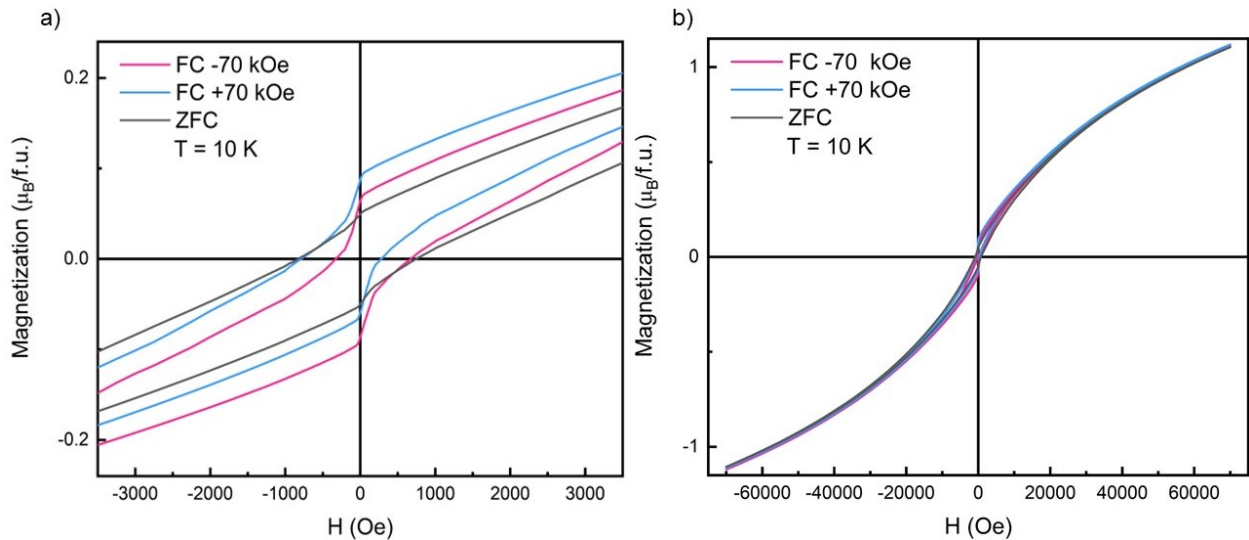


Figure 13: (a) The positive and negative FC MvH is plotted against the ZFC MvH of the same sample at 10K. The residual field is higher for both of the FC's, regardless of polarity, than the ZFC showing pinning in both FC's. b) The full  $\pm 70$  kOe MvH is shown for all three measurements.

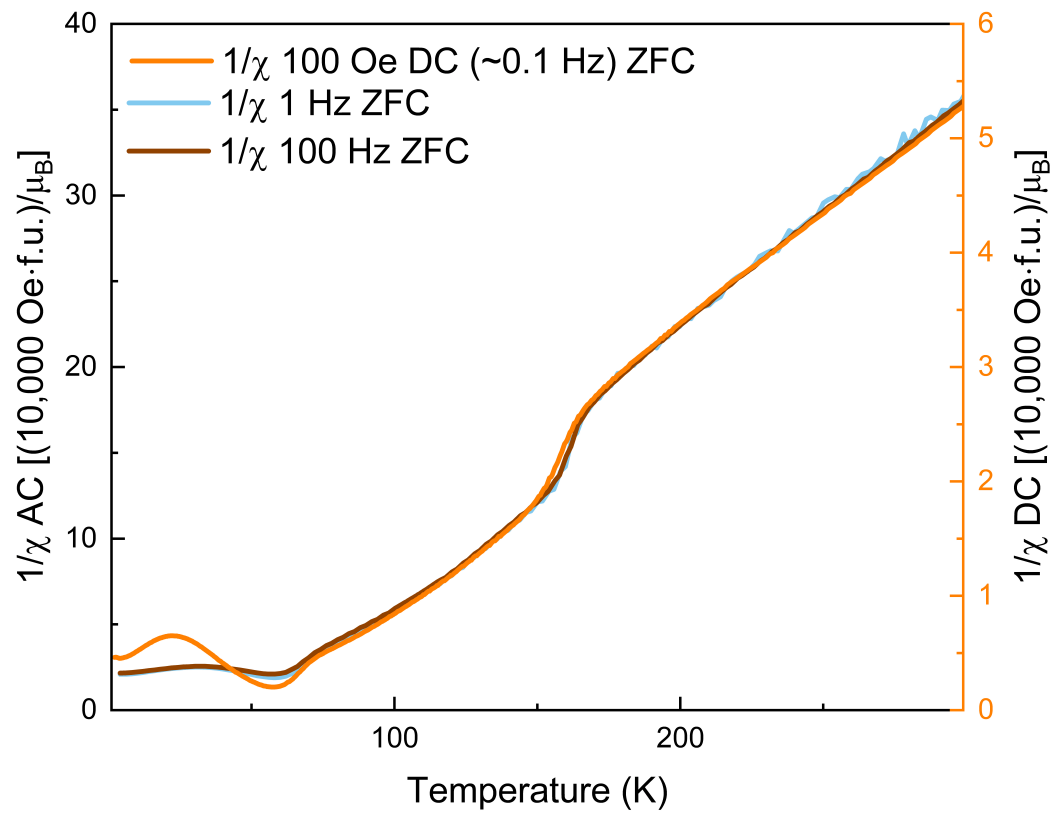


Figure 14: Inverse AC susceptibility at 1 Hz and 100 Hz each with 2 Oe AC-field amplitudes compared to the inverse DC susceptibility calculated from 100 Oe zero-field cooled MvT.

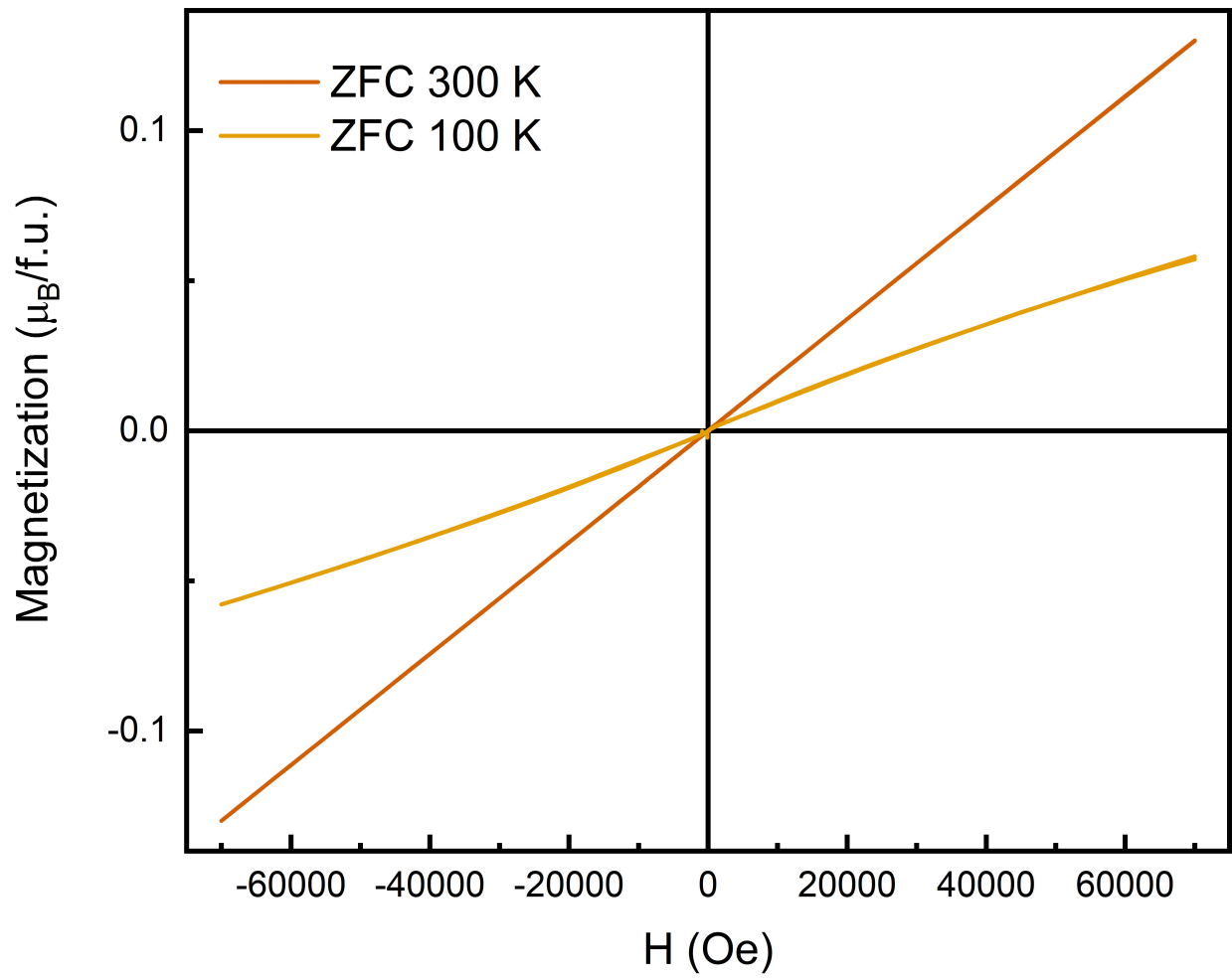


Figure 15: ZFC MvH at 300K and 100K showing a paramagnetic response to applied field.

## References

- [1] B. H. Toby and R. B. Von Dreele, *J. Appl. Crystallogr.*, 2013, **46**, 544–549.
- [2] E. Zolotoyabko, *J. Appl. Crystallogr.*, 2009, **42**, 513–518.
- [3] B. H. Toby, *Powder Diffr.*, 2006, **21**, 67–70.
- [4] A. Munoz, J. A. Alonso, M. J. Martinez-Lope, M. T. Casais, J. L. Martinez and M. T. Fernandez-Diaz, *Phys. Rev. B*, 2000, **62**, 9498–9510.
- [5] A. Muñoz, J. A. Alonso, M. T. Casais, M. J. Martínez-Lope, J. L. Martínez and M. T. Fernández-Díaz, *J. Phys. Condens. Matter*, 2002, **14**, 3285–3294.
- [6] B. Lorenz, *Condens. Matter Phys.*, 2013, **2013**, 1–43.
- [7] A. Muñoz, J. A. Alonso, M. J. Martínez-Lope, J. L. García-Muñoz and M. T. Fernández-Díaz, *J. Phys. Condens. Matter*, 2000, **12**, 1361–1376.